Materials Horizons

Local chemical fluctuation mediated ultra-sluggish martensitic transformation in high-entropy intermetallics

Journal:	*Materials Horizons*
Manuscript ID	MH-COM-10-2021-001612.R2
Article Type:	Communication
Date Submitted by the Author:	22-Nov-2021

Complete List of Authors:	Wu, Y.; University of Science and Technology Beijing, Zhang, Fei; University of Science and Technology Beijing Li, Fengshou; University of Science and Technology Beijing Yang, Yi; University of Science and Technology Beijing Zhu, Jiaming; Shandong University, Civil Engineering Wu, Hong-Hui; University of Science and Technology Beijing, School of Materials Science and Engineering; University of Nebraska-Lincoln , Department of Chemistry Zhang, Yao; University of Science and Technology Beijing Qu, Ruitao; Institute of Metal Research Chinese Academy of Sciences Zhang, Z. F.; Institute of Metal Research Chinese Academy of Sciences Nie, Zhihua; Beijing Institute of Technology Ren, Yang; Argonne National Laboratory, Wang, Yandong; University of Science and Technology Beijing Liu, X. J.; University of Science and Technology Beijing, State Key Laboratory for Advanced Metals and Materials Wang, Hui; University of Science and Technology Beijing, Lu, Z. P.; University of Science and Technology Beijing,

New Concepts for

Local chemical fluctuation mediated ultra-sluggish martensitic transformation in high-entropy intermetallics

Yuan Wu[1], Fei Zhang[1], Fengshou Li[1], Yi Yang[1], Jiaming Zhu[2], Hong-Hui Wu[1], Yao Zhang[1], Ruitao Qu[3], Zhefeng Zhang[3], Zhihua Nie[4], Yang Ren[5], Yandong Wang[1], Xiongjun Liu[1], Hui Wang[1], Zhaoping Lu[1,]*

[1] *Beijing Advanced Innovation Center for Materials Genome Engineering, State Key Laboratory for Advanced Metals and Materials, University of Science and Technology Beijing, Beijing 100083, China*

[2] *School of Civil Engineering, Shandong University, Jinan 250012, China*

[3] *Laboratory of Fatigue and Fracture for Materials, Institute of Metal Research, Chinese Academy of Sciences, Shenyang 110016, PR China*

[4] *School of materials science and engineering, Beijing Institute of Technology, Beijing 100081, China*

[5] *Department of Physics, City University of Hong Kong, 83 Tat Chee Avenue, Kowloon, Hong Kong, China*

** Correspondence and requests for materials should be addressed to Z. P. Lu (Email: luzp@ustb.edu.cn)*

For the first time, we discovered low-temperature superelastic behavior of high-entropy intermetallics and revealed effects of configuration entropy on the related martensitic transformation. We found that the structural features resulted from high configuration entropy, i.e., the lattice complexation and local chemical fluctuations, lead to nano-scale elastic confinement, which retards the stress-induced martensitic transition with an increased critical stress and a small temperature sensitivity over a wide temperature range. As a result, novel superelastic alloys with a unique combination of high critical stress over 500 MPa, high fracture strength of over 2700

MPa, and small temperature sensitivity of superelasticity stress over a wide range of temperature over 220 K in the cryogenic temperature regime was developed.

Local chemical fluctuation mediated ultra-sluggish martensitic transformation in high-entropy intermetallics

Yuan Wu[a], Fei Zhang[a], Fengshou Li[a],Yi Yang[a], Jiaming Zhu[b], Hong-Hui Wu[a], Yao Zhang[a], Ruitao Qu[c], Zhefeng Zhang[c], Zhihua Nie[d], Yang Ren[e], Yandong Wang[a], Xiongjun Liu[a], Hui Wang[a], Zhaoping Lu*[a]

[a] *Beijing Advanced Innovation Center for Materials Genome Engineering, State Key Laboratory for Advanced Metals and Materials, University of Science and Technology Beijing, Beijing 100083, China*
[b] *School of Civil Engineering, Shandong University, Jinan 250012, China*
[c] *Laboratory of Fatigue and Fracture for Materials, Institute of Metal Research, Chinese Academy of Sciences, Shenyang 110016, PR China*
[d] *School of materials science and engineering, Beijing Institute of Technology, Beijing 100081, China*
[e] *Department of Physics, City University of Hong Kong, 83 Tat Chee Avenue, Kowloon, Hong Kong, China*

* *Correspondence and requests for materials should be addressed to Z. P. Lu (Email: luzp@ustb.edu.cn)*

Superelasticity associated with the martensitic transformation has found a broad range of engineering applications such as low-temperature devices in aerospace industry. Nevertheless, the narrow working temperature range and strong temperature sensitivity of the first-order phase transformation significantly hinder the usage of smart metallic components in many critical areas. Here, we scrutinized phase transformation behavior and mechanical properties of multicomponent B2-structured intermetallic compounds. Strikingly, the $(TiZrHfCuNi)_{83.3}Co_{16.7}$ high-entropy intermetallics (HEI) shows superelasticity with high critical stress over 500 MPa, high fracture strength of over 2700 MPa, and small temperature sensitivity in a wide range of temperature over 220 K. The complex sublattice occupation in these HEIs facilitates formation of nano-scaled local chemical fluctuation and then elastic confinement, which leads to an ultra-sluggish martensitic transformation. The thermal activation of the martensitic transformation was fully suppressed while the stress activation is severely retarded with an enhanced threshold stress over a wide temperature range. Moreover, the high configurational entropy also results in a small entropy change during phase transformation, consequently giving rise to the low temperature sensitivity of the superelasticity stress. Our findings may provide a new paradigm for development of advanced superelastic alloys, and shed new insights into understanding of martensitic transformation in general.

Introduction

A variety of high-performance engineering applications at low temperature, ranging from deep-space to polar region exploration, requires metallic components to withstand large yet reversible deformation over a broad temperature range.[1-4]. For instance, superelastic alloys (SAs) in spacecrafts for Mars and moon typically work at the temperature of 80 to 400 K and need to be as strong as possible. However, the elastic strain limit governed by the yield stress and Young's modulus rarely exceeds 1% due to the intrinsic restriction of atomic bonding in metals.[5] In contrast, a large recoverable pseudo-elastic strain (>2%) can be achieved in the alloys exhibiting the stress-induced diffusionless structural transformation (i.e., the so-called martensitic transformation), such as NiTi-,[3] Fe-,[6-8] and Cu-[9]based alloys, which is also referred to as superelasticity. The cubic unit cells of the parent phase spontaneously undergo the same distortion over a very long range (called long-range ordering of the strains) upon loading and hence form a distorted lattice called martensite.[3] The nature of the first-order stress-induced martensitic transformation gives rise to a strong temperature dependence in a narrow temperature range of the superelasticity. To meet the engineering requirements for SAs, characteristics of the diffusionless phase transformation, including increase of the working temperature range, reduction of temperature dependence and increase of the threshold stress need to be carefully tailored.[7, 10-12]

Serious efforts have been devoted to understanding the involved martensitic transformation (MT) and the influencing factors in SAs. It was found that crystalline defects such as vacancies play important roles in long-range strain ordering.[13] By adding 1.5 at.% excess Ni into a martensitic stoichiometric compound $Ti_{50}Ni_{50}$, for example, long-range strain ordering in the transformed martensite was destroyed due to the random distribution of point defects and multiple possibilities to form strain variants. As a result, a strain glass behavior was observed,[14-17] i.e., the MT could only be activated by mechanical stress, but not by temperature

change (no transformation down to 4.2 K).[14, 15] To develop low-temperature SAs with improved properties, therefore, novel effective approaches for controlling defects and local structural heterogeneity in SAs are urgently required.

Recently, a new alloy design concept, i.e., high-entropy alloys (HEAs), based on the consideration of maximizing the configuration entropy to stabilize single solid solution phases was proposed.[18, 19] The high configuration entropy endows HEAs unique structural characteristics, such as large lattice distortion and local chemical fluctuations, which significantly enhances resistance to plastic deformation.[20-22] It is argued that these structural characteristics could change local defect states,[23-25] and may provide an effective way to tailor diffusionless martensitic transformation behavior of SAs.[26, 27] Indeed, high-temperature shape memory (SM) behavior was first reported in the TiZrHfCoNiCu high-entropy intermetallics (HEI) with a low amount of Co and a high amount of Ni and/or Cu.[28, 29] In this study, we systematically investigated low-temperature phase transformation and deformation behavior of the $(TiZrHfCuNi)_{100-x}Co_x$ (x=13~23 at.%) HEIs. Strikingly, a unique combination of high critical stress over 500 MPa, high fracture strength of over 2700 MPa, and small temperature sensitivity of superelasticity stress over a wide range of temperature over 220 K down to cryogenic temperature regime was revealed in the TiZrHfCuNiCo HEI for the first time. An ultra-sluggish martensitic transformation resulted from local chemical fluctuations at the nano-meter scale was found to be mainly responsible for the unique SA characteristics.

Results and Discussion

Superelastic behavior at different temperatures

A series of $(TiZrHfCuNi)_{100-x}Co_x$ HEIs were fabricated, and it was found that a B2 phase with the space group of *Pm*-3*m* was obtained when the Co content is higher than 15% (**Figure S1**), which is similar to that of binary TiNi,[30] CuZr,[31] and CoHf[32] alloys. To elucidate

superelastic and phase transformation behavior in the current HEIs, results of the as-prepared $(TiZrHfCuNi)_{83.3}Co_{16.7}$ (termed as Co16.7 hereafter) HEI are presented in detail as an example. SEM images of Co16.7 shows a single phase with a grain size of around 10 μm, and neither secondary phase nor precipitation was found (**Figure S2**). Representative TEM image and the corresponding area electron diffraction (**Figure S3**) verify the single B2 structure. Nevertheless, distinct contrast at the nanometer scale was observed, which implies existence of strong nano-scale chemical fluctuation despite the single B2 structure.

The cyclic stress-strain curves for the specimens tested at 77, 173, 298 and 373 K are shown in **Figures 1**a-1d, respectively. At each temperature, the specimens were firstly loaded under compression to a strain of 1% and then unloaded, followed by reloading up to 3% and then unloading in the second cycle, and so forth with a strain interval of around 2%. When loaded at the cryogenic temperatures, the specimens exhibit "flag-shaped" stress-strain behavior characteristically, similar to that observed in conventional superelastic alloys.[33, 34] At the liquid nitrogen temperature of 77 K, the current HEI yields at about 500 MPa, followed by a sigmoidal stress-strain behavior which is typical for SAs. After the release of load, the specimen shows a recoverable strain of 4.3% that includes both ordinary elastic strain and superelastic strain. Usually, the superelastic strain ε_{SE}^{i} (i is the number of cycles) is defined as $\varepsilon_{SE}^{i} = \varepsilon_{a}^{i} - \varepsilon_{e}^{i} - \varepsilon_{r}^{i}$, where ε_{a}^{i} is the applied strain to the specimen, ε_{e}^{i} is the ordinary elastic strain and ε_{r}^{i} is the residual strain after removal of the stress. The superelastic strain of the current HEI was found to increase with the increase of applied strain and eventually saturate at the maximum value of about 3.3% (see the inset in **Figure 2**a), which is similar to that of a β-type Ti-based superelastic alloy.[35] It should be noted that the elastic modulus (estimated from the slope of elastic stage) slightly increased with the loading cycles, implying a structure change during the cyclic loading.

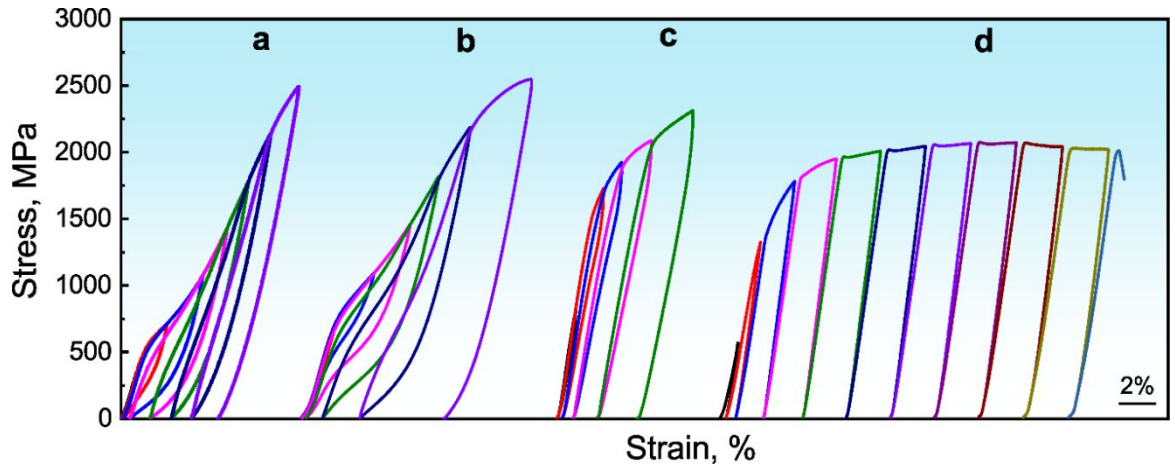

Figure 1. Loading-unloading stress-strain curves tested at the temperature of 77K (a), 173K (b), 298K (c) and 373K (d).

At room temperature, the current HEI yields at about 1400 MPa with linear elasticity about 2%. The sample shows total recovery strain of 2%, and during the subsequent loading cycle, a linear stress-strain relationship was observed. The linear elastic strain increases with the increase of applied loading, and the plastic strain is partly recovered in the late cycles, suggesting an apparent anelastic behavior. The recoverable strain keeps increasing as the loading strain is increased. It should be noted that at room temperature, the current HEI shows the linear super-elasticity, instead of the pseudo elasticity reported previously in conventional SAs such as TiNi and CuZr. At the elevated temperature of 373 K, the plastic deformation was completely retained when the applied stress is released (**Figure 1**d), indicating that there is no superelasticity during deformation.

Variation of superelasticity with temperature is illustrated in **Figure 2**a, from which it is clear that the current HEI exhibits superelasticity over a temperature range from 77 K to room temperature (i.e., the total temperature interval for the superelastic deformation exceeds 220 K), and the superelasticity appreciably increases with the decrease of temperature. The threshold stress for the martensitic transformation, i.e., the yield strength, and the fracture strength as a function of testing temperatures are shown in **Figure 2**b. As can be seen, the

fracture strength monotonically decreases with the increase of testing temperature, whereas the yield strength first increases in the cryogenic temperature regime and then decreases with the temperature in the regime above room temperature, suggesting a transition of deformation mechanism. In comparison with the low-entropy binary TiNi and TiNb SAs which show superelasticity at above room temperature (see **Figure** 2b), the current HEI shows superelasticity not only in a wide temperature span of over 220 K, but also smaller temperature sensitivity of the superelasticity stress (i.e., the slope of the lines). Furthermore, the current HEI exhibits high yield strength of 500 MPa and ultimate strength up to 2700 MPa at cryogenic temperatures, which are the highest ever reported. Large threshold stress, high fracture strength, wide transformation temperature range and small temperature sensitivity of the MT make the current HEI unique among all SAs, especially for cryogenic applications.

In conventional SAs, it is well accepted that the Clausius-Clapeyron relationship,[36] expressed as $\frac{d\sigma_y}{dT} = -\Delta S/\varepsilon$, where ΔS is the entropy change of the transformation per unit volume and ε is transformation strain,[37, 38] can describe temperature dependence of the transition stress for the MT. A linear relationship between the yield strength and the testing temperature, as observed in **Figure 2**b, suggests that the Clausius-Clapeyron relationship is also valid for the present HEI. Based on **Figure 2**b, the $\frac{d\sigma_y}{dT}$ value, i.e., the slope of the curves, can be estimated to be 3.3 MPa/K. Thus, the entropy change ΔS for the stress-induced MT in this HEI can be determined to be -3.38 J/mol K with a maximum strain of 3.5%, which is much smaller than that of the binary TiNi (-4.37 J/mol K)[39] and Fe-Ni (-6.28 J/mol K)[40] alloys with the same structural transformation path from B2 to B19', implying that the higher configurational entropy leads to the lower entropy change of the phase transformation. In other words, such low entropy change resulted from high configuration entropy could be responsible for the small temperature sensitivity of the superelasticity stress.

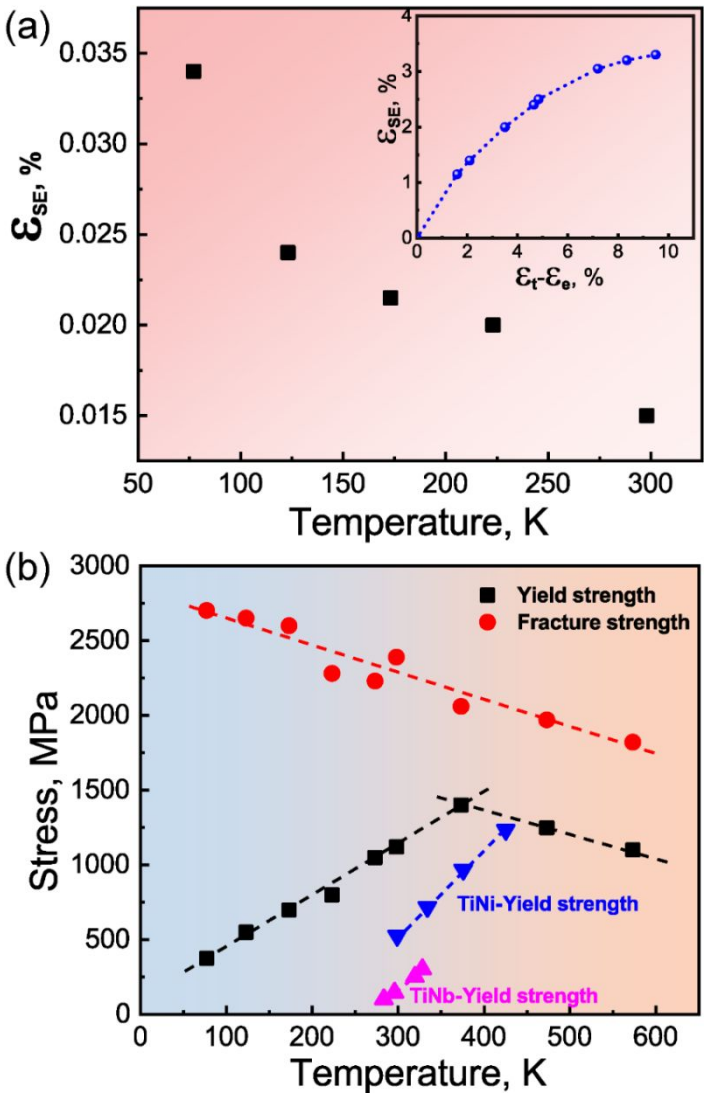

Figure 2. Temperature dependence of superelasticity (a), superelastic stress and fracture strength (b) in the Co16.7 HEI. Inset in (a) is the variation of superelasticity with loading strain at 77K. Variation of superelastic stress of the TiNi and TiNb SAs with temperature was also shown in (b) for comparison. The current HEI has a higher superelastic stress over a wide range of temperature.

Structure evolution during phase transformation

To investigate structural evolution upon loading of the current HEI, in-situ high energy X-ray diffraction experiments under loading-unloading were conducted at both room temperature and cryogenic temperatures. As an illustration, the synchrotron diffraction patterns of in-situ loading-unloading at 213K and room temperature are shown in **Figure 3**a and **Figure 3**b,

respectively. As the deformation proceeds, diffraction peaks of the B2 phase shift toward the small *d* spacing, but the peak intensity and width keep nearly unchanged prior to the macroscopic yielding. Notably, right after the macroscopic yielding, the intensity of the B2 peaks starts to decrease and a few extra peaks (indexed as B19') appear,[41, 42] **Figures 3**c, d and e show the peak intensity, lattice strain and FWHM (full width at the half maximum) of the $(110)_{B2}$ and $(020)_{B19'}$ planes, respectively. Evidently, a MT from B2 to B19' accounts for the macroscopic yielding. The intensity of the B19' peaks gradually increases with further loading and becomes dominant at the maximum stress. Note that the intensity of B2 does not totally recover after unloading, indicating a partial reversible phase transformation (see **Figure 3**c). Lattice strain (**Figure 3**d) of the B2 phase increases linearly in the elastic stage while deviates after yielding (i.e., formation of B19'), which suggests occurrence of loading partition between the parent B2 and product B19' phases. After completely unloading, the lattice strain of B2 keeps negative while that of B19' becomes positive with subject to its original state, indicating residue of the internal stress between B2 and B19' phases even after the release of the external stress. The peak width of B2 remains almost unchanged during the elastic deformation stage and gradually increases after yielding (i.e., start of phase transformation). Upon unloading, the FWHM value of both B2 and B19' decreases firstly but increases again below 800 MPa (**Figure 3**e). Generally, homogeneous strains only cause peak shift, whilst the local fluctuation in strains leads to peak shift and broadening.[43, 44] These in-situ loading results confirm that short-range fluctuation in the strain field was developed during phase transformation upon loading and the partial reversible transformation during unloading. More interestingly, the sluggish change of the scattering intensity of the B19' phase during both loading and unloading was observed (see **Figures 3**b and **3**c), indicating a continuous volume variation of the martensitic phase in this HEI. This behavior is in sharp contrast to the scenario of conventional MT in typical SAs, which usually happens in an avalanche-like manner.

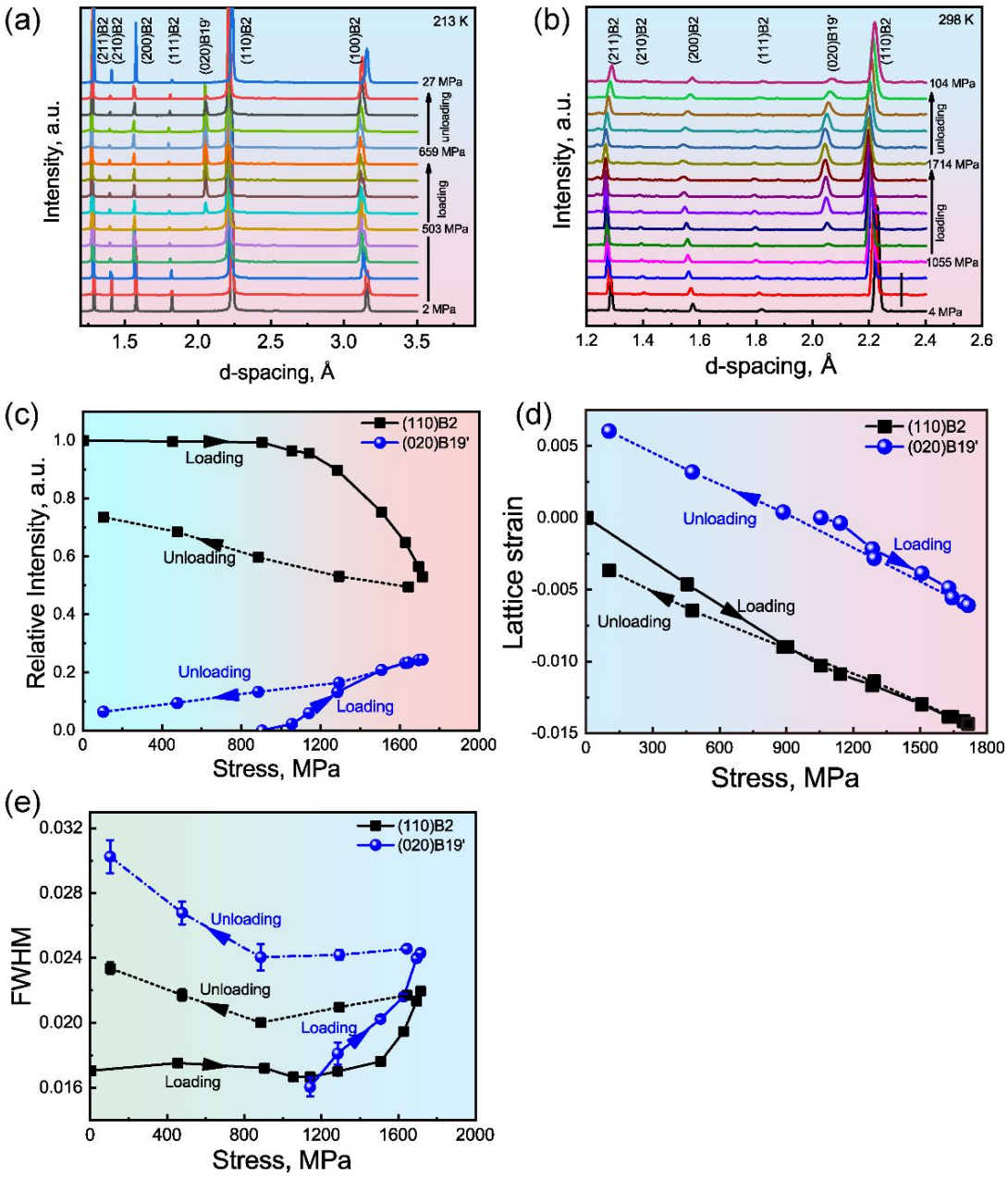

Figure 3. *In-situ* synchrotron diffraction loading data of the Co16.7 HEI. Evolution of the diffraction patterns at 213K (a) and room temperature (b) during loading-unloading. Evolution of peak intensity (c), lattice strain (d) and FWHM (full width at the half maximum, e) during loading-unloading at room temperature.

Although stress-induced MT in the current HEI was clearly observed at the temperatures below 298 K, no thermal-induced transformation was detected upon cooling. In-situ high energy X-ray diffraction patterns over a wide temperature range from 383 to 93 K (**Figure S4**) show no change in the diffraction peaks over the entire temperature range, confirming no

occurrence of phase transformation. Similarly, no signal of any MT was noticed by the DSC measurement from 300 to 110 K (**Figure S5**). These results verify that the MT of the current HEA can be activated mechanically, but not thermally, verifying that superelasticity due solely to a stress-induced MT. To explore the origins of the unique MT behavior in the current HEA, atomic scale structural characterization was conducted, and the corresponding phase field simulation was also carried out based on the Landau theory in which the change of ordering parameter can affect the variation in energy landscape.

Complex sublattice occupation and formation of nano-scale local chemical fluctuation

Microstructure characterization reveals that the as-cast sample of Co16.7 has a grain size of around 10 μm. Grain interiors were found to be slightly enriched of Co, Ni and Hf while grain boundaries were enriched with Ti, Zr and Cu atoms (**Figure S2**), which may be caused by the consititutional supercooling during solidifaction[45]. Inside each grain, distinct contrast at the nanometer scale was observed, as shown in the TEM image (**Figure S3**). To further characterize such chemical heterogeneity, APT tests of this specific sample were conducted, and the results are shown in **Figure 4**. As can be seen, chemical fluctuation actually occurred at the two length scales; one is at the length scale from tens to hundred nanometers with a plate-like shape, consisting of Hf-rich and NiCo-rich layers (**Figure 4**a and **4**b). Inside each kind of layers, the other non-uniformity in the composition was also observed. Hf-rich and NiCo-rich domains of around 5 nm in size and approximately equiaxed in shape are clearly seen from the 3D atomic distribution and the corresponding 2D contours of Hf, Ni and Co (see **Figure 4**c). To sum up, the current HEI can be regarded as a unique architecture consisting of local compositional segregation regions at multiple length scales. It has been proposed that the chemical fluctuations at small scales (usually <15 nm) can strongly affect MT behavior, but those at a large scale not[46]. Therefore, we place the emphasis on the effects of nano-scale

compositional fluctuations in the current study. The Hf-rich and NiCo-rich regions have different potency of MT and then may confine with each other,[47] which could be responsible for the observed unique characteristics of the current HEI.

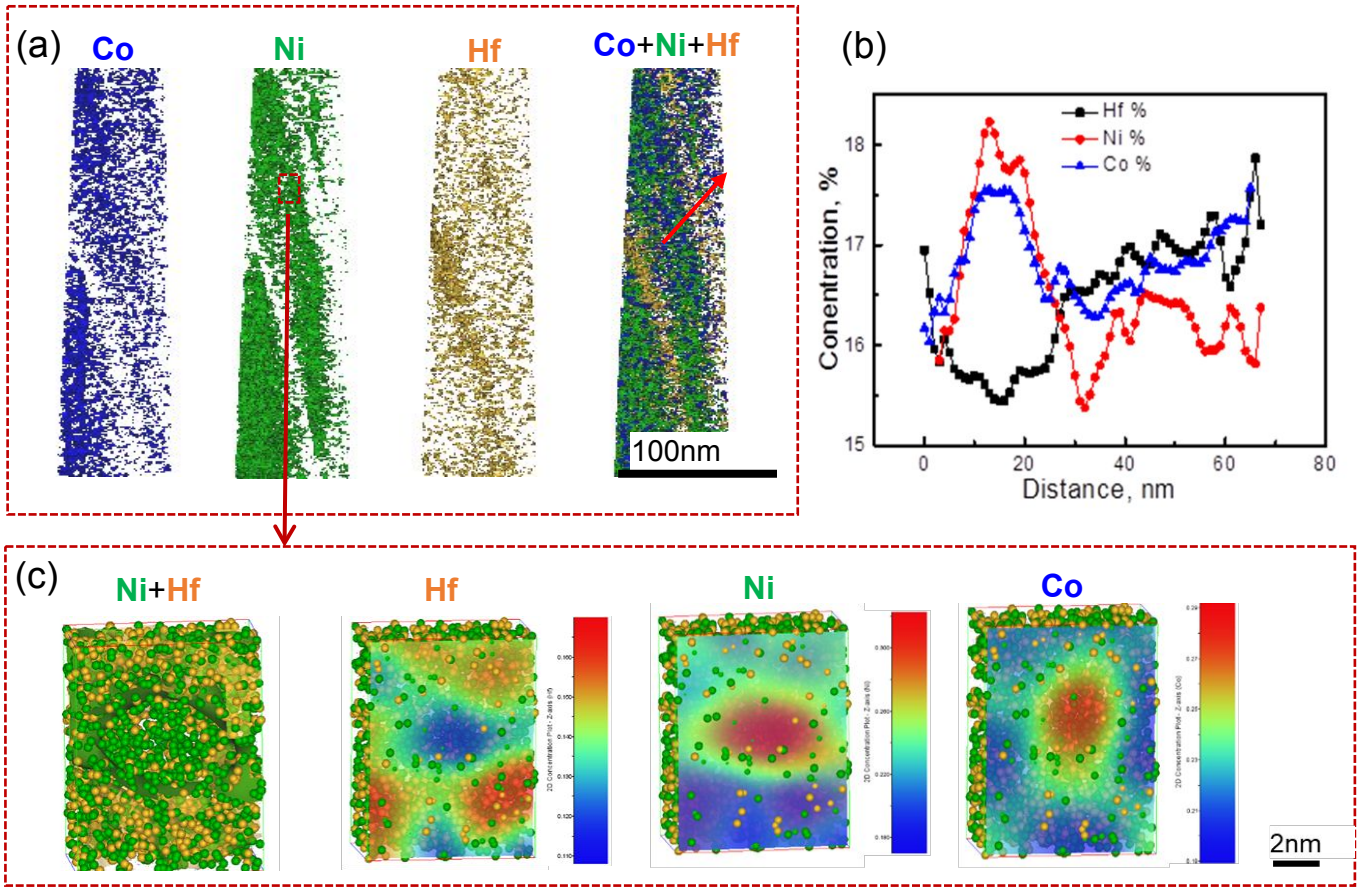

Figure 4. Atom probe analysis showing nano-scale chemical heterogeneity in the current Co16.7 HEI. 3D iso-concentration surfaces of 23.5% Co, 21% Ni, 18.5% Hf and 23.5%Co+21%Ni+18.5%Hf (a) showing the layers with composition modulation at tens of nanometers. (b) proximity histogram showing the composition change along the arrow in (a). (c) Atomic distribution of a representative local region, with 21% Ni and 18.5% Hf isosurfaces overlapped, showing chemical heterogeneity with a size of around 5 nm. Only Ni and Hf atoms were shown and other elements were hidden for a simplified illustration. 2D contours of elemental distribution; Hf, Ni and Co, domains with a size of about 5 nm were seen. The distribution trend of Ni is similar to that of Co, but opposite to that of Hf.

To understand formation mechanism of the above strong chemical heterogeneity, the atomic occupation was analyzed by the Retvield refinement of the neutron diffraction data, as

shown in Figure S6. Atoms of Ti, Zr, and Hf were identified to occupy one sublattice while those of Co, Cu and Ni on the other, suggesting an ordering AB-type B2 structure but with random distribution of each group of three elements on either specific sublattice. The configurational entropy in this HEI can be calculated by the modified Boltzmann equation with consideration of the HEI microstructure which contains two different sublattices.[48]

$$\Delta S_{conf} = -R\left\{\frac{N_h}{N_t}\sum_{i=1}^{n_h} h_i \ln(h_i) + \frac{N_k}{N_t}\sum_{j=1}^{n_k} k_j \ln(k_j)\right\} \quad (1)$$

Where h represents one sublattice with a number of sites N_h, whilst k represents another sublattice with a number of sites N_k, $N_t = N_h + N_k$, where R is the ideal gas constant of 8.314 J/(mol K), n_h and n_k are the elements species in the sublattice h and k, respectively, and h_i and k_j are the molar fraction of the constituent i and j in the sublattice h and k, respectively. In the current HEI with three elements on either sublattice, the configurational entropy can be calculated as 1.098R, which is obviously much higher than the binary B2 phase. In conventional binary SAs such as TiNi and CuZr with a B2 structure, each sublattice was strictly occupied by a specific element. While in the current HEI with three elements on one sublattice, multiple possibilities of sublattice occupation could facilitate formation of nano-scale local chemical fluctuation. Furthermore, our recent work indicated that formation of local chemical ordering can lower the system energy and thus stabilize the HEA lattice[49, 50]. Therefore, the formation of the nanoscale segregationcould be driven by the free energy reduction due to the enthalpy effect in the current HEI.

Effects of nano-scale local chemical fluctuation on the unique martensitic transformation behavior

To reveal origins of the MT characteristics in the current HEI, the unique nano-scale compositional architecture was then input into a phase field model and the corresponding results

are shown in **Figure 5**. The phase field model is formulated based on the Landau theory,[51] gradient thermodynamics,[52, 53] and Khachaturyan–Shatalov's microelasticity theory of structural phase transformations.[54] It is noteworthy that the influences of nano-scale chemical fluctuation on the phase stability and the transformation strains are considered in our model.[55-57] The details about the phase field model can be found in Materials and Methods section. The variation of Landau free energy f_{ch} with temperature is shown in **Figure 5**a. Although the stability of the martensite in a local region increases with the decrease of temperature, the symmetry of the free energy curve was not broken and the energy barrier of MT is always higher than the thermal energy, which makes it impossible for thermal-induced MT. The case at 173 K as an example is shown in **Figure 5**c, and as can be seen, no MT was observed during cooling from 175 to 75 K, which is consistent with the DSC results (Figure S5). According to the Landau theory,[58] nevertheless, the external stress can "tilt" the free energy curve as a result of the stress-strain coupling energy (**Figure 5**b). The physical picture is that external stress tends to stabilize a macroscopic strain state with a suitable non-zero average strain. The occurrence of forward and backward MT is determined by the relative free energy between the parent and martensitic phases. When applying an external load which equals to the critical stress of MT, the free energy of martensite becomes lower than that of the parent phase, then the forward MT happens. When the external load decreases to a certain value, the free energy of the parent phase becomes lower than that of the martensitic phase, then the martensite would transform back to the parent phase. As an example, the simulated case at 173 K is shown in **Figure 5**d. The MT occurs and the volume fraction of martensite increases with loading above 800 MPa. During unloading, the martensite transforms back to the austenite, which is consistent with the experimental observation.

Furthermore, due to the varied transformation tendency of different local regions and multiple possibilities to form strain variants, self-organization and collective growth of the

strain variants to form a long-range strain ordering can thus be suppressed. Based on our phase field model, evolution of microstructure of the current HEA upon loading is simulated as shown in **Figure 5**e. First, only 8 of the 12 possible variants were observed during the loading process, implying that some variants are unstable and cannot be activated by the external stress up to 1000 MPa. Second, the martensitic variants are confined at the nanoscale and formation of large martensitic laths which are usually observed in conventional SAs, was not observed, indicating that the nano-scale chemical fluctuation has dramatic effects on the MT. The Hf-rich regions which have a much lower onset temperature of MT are more stable, and then elastically confine the MT in the neighboring NiCo-rich layers. Such nano-scale elastic confinement suppresses the autocatalysis for rapid growth of the martensitic laths and retards the MT, which also necessarily increases the critical stress for MT. The nano-scale elastic confinement would inevitably cause nano-scale internal stress between local regions with chemical fluctuations, which gives rise to the peak broadening as shown in **Figure 3**e. Consequently, the nano-scale chemical fluctuation and the subsequently developed nano-scale local strain heterogeneity upon loading have determinative effects on sluggish characteristics of the MT in the current HEI. Upon further deformation, the nano-scale martensitic variants grew up via coarsening and thus, the martensite laths formed. Therefore, in contrast with conventional SAs such as TiNi which exhibit typical strong first-order (discontinuous) phase transformation, the current HEI shows a weak first-order (continuous) phase transformation and a prolonged phase transformation process.

Therefore, effects of high configuration entropy in the current multicomponent intermetallic compound on phase transformation might be twofold; one is the reduction of the entropy of transformation, which helps to lower the temperature sensitivity of critical superelasticity stress, i.e., the critical superelasticity stress increases much slowly than conventional SAs as the temperature changes. The other is the suppression of the autocatalysis

of rapid growth of transformed martensite resulted from the nano-scale chemical fluctuations, which leads to a sluggish transformation process and prolongs the transformation temperature range. It should be noted that other factors caused by the high configuration entropy cannot be fully ruled out, such as the wide range of formation enthalpy of point defects which may stem from the larger lattice distortion of the HEI. The point defects could also break the symmetry of the Landau potential and then alter the global thermodynamic stability of the martensite, thus influencing the MT behavior of the HEA.

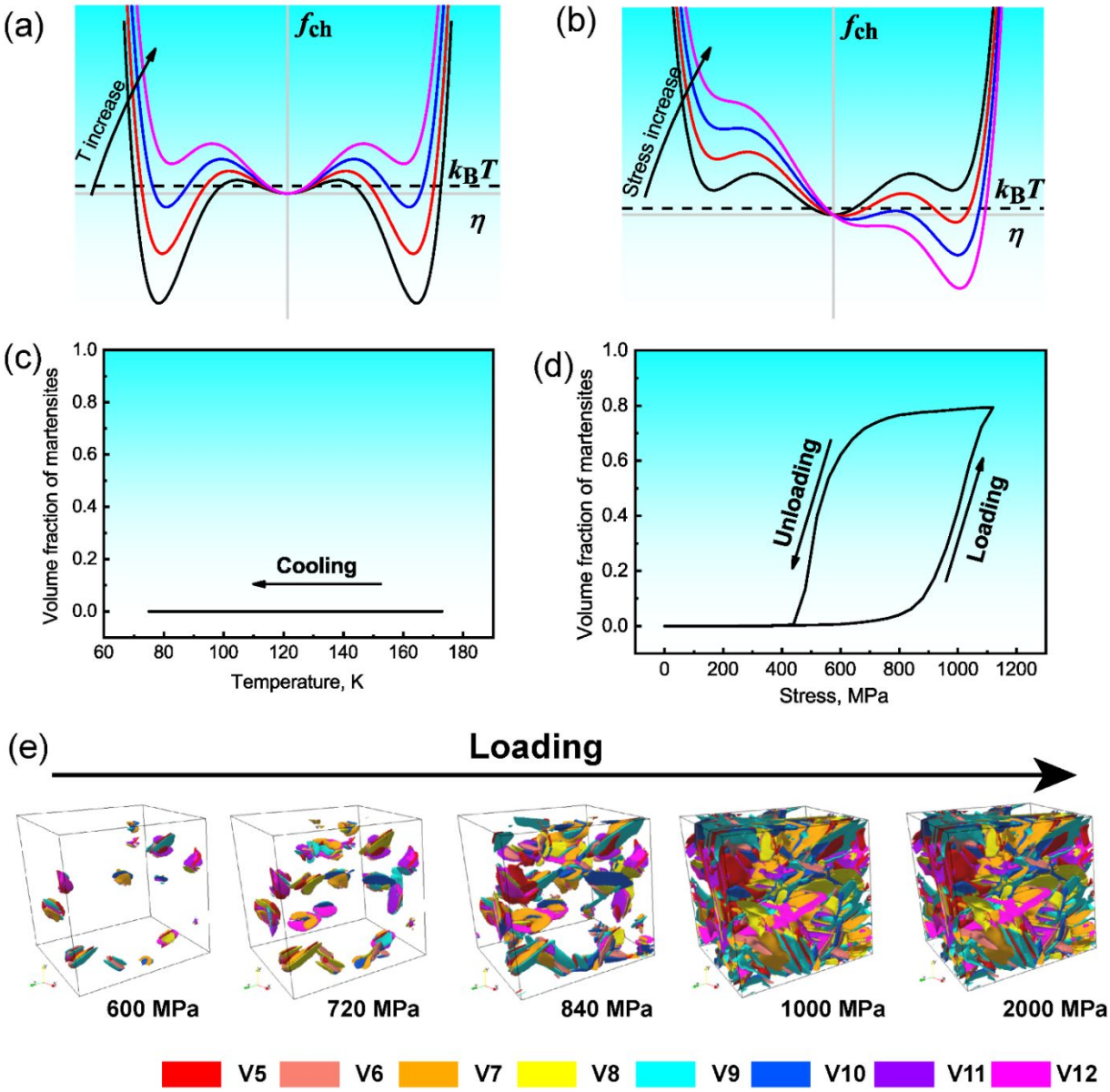

Figure 5. Phase field model showing the characteristics of phase transformation of Co16.7 HEI. Variation of Landau free energy, f_{ch}, of a volume element with the temperature (a) and stress (b). The Landau free energy curves keep symmetrical with temperature change while become tilted with applying stress. Evolution of the volume fraction of martensite during cooling (c) and loading-unloading (d), indicating that the martensitic transformation was solely stress-induced. Evolution of martensitic variants with external loading (e), suggesting that the rapid growth of martensite was suppressed and the martensitic variants were found to be confined within the nano-scale.

Conclusion

In summary, low-temperature superealstic behavior was first reported in B2-structured HEIs with atoms of Ti, Zr and Hf on one sublattice and those of Co, Cu and Ni on the other sublattice. Specifically, the equimolar Co16.7 HEI shows superelasticity with high critical stress over 500 MPa within a wide temperature range of over 220 K. The complex lattice occupation facilitates formation of nano-scale chemical fluctuations and elastic confinement, which results in the sluggish martensitic transformation. Consequently, the stress-induced MT is retarded with an increased critical stress, along with suppression of thermal-induced MT. It was revealed that the high configurational entropy of the current HEI led to a lower entropic change of phase transformation and subsequently a smaller temperature sensitivity of the threshold stress. Our current work may not only shed lights on understanding of MT behavior in general, but also provide a reliable approach for development of novel SAs with unique properties via the entropy stabilization concept.

Experimental Section

Materials

Alloy ingots with a nominal composition of $(TiZrHfCuNi)_{100-x}Co_x$ (x=13~23 at.%) were prepared by arc-melting a mixture of pure metals with purity over 99.9 at% in a Ti-gettered

argon atmosphere. All ingots were remelted at least five times to eliminate chemical imhomogeneity. Cylindrical samples with a diameter of 6 mm and length of 60 mm were fabricated by suction casting with a copper mold. Compression samples with a diameter of 3 mm and length of 6 mm were cut from the rods by electrical discharge machining.

Characterization

Compressive tests at room temperature were performed on a CMT4105 universal electronic testing machine at the strain rate of 1×10^{-3} s^{-1}, whilst the tests at low temperatures (i.e., 223, 173, 123 and 77 K) were performed on a CMT5105S universal electronic testing machine at the strain rate of 2×10^{-4} s^{-1}. Phase constitution of the as-cast alloys was characterized by using an X-ray diffractometer with CuKα radiation. Microstructure of these alloys was characterized by using a Zeiss SUPRA55 field-emission scanning electron microscope (SEM) equipped with energy-dispersive spectrometry, and a JEM-2100 transmission electron microscope (TEM) operated at 200 kV. The *in-situ* synchrotron high-energy X-ray diffraction (HEXRD) measurements under cooling and loading at cryogenic temperatures were carried out at the 11-IDC beamline of Advanced Photon Source, Argonne National Laboratory. A monochromatic X-ray beam with a wavelength λ=0.11798 Å was used, and the 2-D diffraction patterns were collected in transmission geometry using a PerkinElmer α-Si flat-panel large-area detector. The 1-D HEXRD patterns were obtained by integrating the 2-D patterns with Fit2D software.[59] Atom probe tomography (APT) analyses were carried out in a Cameca LEAP 5000XR under ultra-high vacuum of approximately 2.5×10^{-11} Torr, at a specimen temperature of 50 K and with a target evaporation rate of 5 ions for 1000 pulses on average in laser pulsing mode at 15 % pulse fraction. The instrument was equipped with a picosecond (<10 ps) ultra-violet laser with a wavelength of λ=355 nm operating at a pulse repetition rate of f_{Pulse}=200 kHz. The APT samples were prepared using standard FIB lift-out procedures[60, 61] utilizing a FEI Quanta 200 3D equipped with an Omniprobe micromanipulator. The lifted-out samples were mounted on Si micro tip coupons. The CAMECA integrated visualization and analysis software IVAS 3.6.8

was used for data analysis and three-dimensional (3D) atomic reconstruction.

Calculation: Phase field model of phase transformation in HEIs

Symmetry breaking in B2 → B19′ phase transformation

The symmetry breaking accompanying B2 → B19′ phase transformation leads to 12 crystallographic equivalent deformation modes characterized by 12 different transformation strain tensors.

Free energy formulation

The total free energy functional, F, of the system is formulated as the following

$$F = \int \left[\frac{1}{2}\kappa \sum_{\mathrm{p}=1}^{12} (\nabla \eta_{\mathrm{p}})^2 + f_{\mathrm{ch}}(\eta_1, \cdots \eta_{12}) + f_{\mathrm{ex}}(\eta_1, \cdots \eta_{12}) \right] d^3\boldsymbol{r} + E_{\mathrm{el}} \qquad (2)$$

where $\kappa = 1 \times 10^{-11}$ J/m is the gradient energy coefficient for structural non-uniformities following the gradient thermodynamics,[52, 53] f_{ch} is the Landau free energy that describes the free energy of a local volume element having a uniform structural state characterized by $\eta_{\mathrm{p}}(\mathbf{r})$ (p=1-12). Then the stress-free transformation strain tensor for a local volume element located at **r** will be given by

$$\varepsilon_{ij}^{MT}(\boldsymbol{r}) = \sum_{p=1}^{12} \varepsilon_{ij}^{0}(p, \boldsymbol{r}) \eta_p^2(\boldsymbol{r}) \qquad (3)$$

and the Landau free energy can be approximated by the following polynomial

$$f_{\mathrm{ch}}(\eta_1, \cdots \eta_{12}) = \frac{1}{2}A_1(T - T_0) \sum_{\mathrm{p}=1}^{12} \eta_{\mathrm{p}}^2(\boldsymbol{r}) - \frac{1}{4}A_2 \sum_{\mathrm{p}=1}^{12} \eta_{\mathrm{p}}^4(\boldsymbol{r}) + \frac{1}{6}A_3 \left(\sum_{\mathrm{p}=1}^{12} \eta_{\mathrm{p}}^2(\boldsymbol{r}) \right)^3 \qquad (4)$$

where A_1=1.39×10^6 J/m^3·K, A_2=1.77×10^8 J/m^3 and A_3=1.84×10^8 J/m^3 are expansion coefficients, $T_0 = 62 - 90\frac{c_v(\boldsymbol{r}) - c_v^0}{0.005}$, *where* $c_v(\boldsymbol{r})$ is the average concentration of valence electron at position $\boldsymbol{r}$, and $c_v^0 = 0.1927$ is the average concentration of valence electron of whole material.[62]

The free energy associated with an external stress, σ_{kl}, (i.e., the work term by the external stress) in Eq. (2) is given by the following equation

$$f_{\mathrm{ex}}(\eta_1, \cdots \eta_{12}) = -\sigma_{\mathrm{kl}} \cdot \varepsilon_{\mathrm{kl}}^{\mathrm{MT}}(\boldsymbol{r}). \qquad (5)$$

The last term in Eq. (2), E_{el}, is the coherency elastic strain energy of a structurally non-uniform but coherent system (i.e., martensitic variants coherently embedded in the parent phase matrix) characterized by $\eta_{\mathrm{p}}(\boldsymbol{r})$. According to a recent study,[56] in which a new mathematical formulation of the coherency elastic strain energy that accounts for CM is derived based on Khachaturyan–Shatalov's microelasticity theory (KS-theory),[54] it has the following close form

$$E_{\mathrm{el}} = \frac{1}{2}\sum_{\mathrm{K}=1}^{9}\sum_{\mathrm{L}=1}^{9}\int \frac{d^3k}{(2\pi)^3} B_{\mathrm{KL}}(\boldsymbol{n})\{\theta_{\mathrm{K}}\}_k\{\theta_{\mathrm{L}}\}_k^*, \qquad (6)$$

where the integral is taken in the reciprocal space, $\boldsymbol{n} = \frac{\boldsymbol{k}}{k}$ is a unit vector and $\boldsymbol{k}$ is a vector with modulus k in the reciprocal space (note that $\boldsymbol{k} = 0$ is to be excluded from the integration), and $\{\theta_{\mathrm{K}}\}_k$ represents the Fourier transformation of θ_{K}, which is defined as $\theta_{\mathrm{K}}(\boldsymbol{r}) = \sum_{\mathrm{p}=1}^{12}\left[\varepsilon_{\mathrm{ij}}^0(\mathrm{p}, \boldsymbol{r}) \cdot \eta_{\mathrm{p}}^2(\boldsymbol{r})\right]$ (the indexes i, j and K in this expression are correlated via a generalized Voigt notation, i.e. 11 →1, 22 →2, 33 →3, 23 →4, 13 →5, 12 →6, 32 →7, 31 →8, 21 →9). Note that the transformation strain, $\varepsilon_{\mathrm{ij}}^0(\mathrm{p}, \boldsymbol{r})$, is a function of position because of its dependence on local concentration[63, 64] (see Fig. 1b). For a system with a free boundary, $B_{\mathrm{KL}}(\boldsymbol{n})$ in Eq. (6) reads

$$B_{\mathrm{KL}}(\boldsymbol{n}) = \begin{cases} 0 & \boldsymbol{n} = 0 \\ C_{\mathrm{ijkl}}\varepsilon_{\mathrm{ij}}^{\mathrm{new}}(\mathrm{K})\varepsilon_{\mathrm{kl}}^{\mathrm{new}}(\mathrm{L}) - n_{\mathrm{i}}\sigma_{\mathrm{ij}}^{\mathrm{new}}(\mathrm{K})\Omega_{\mathrm{jk}}(\boldsymbol{n})\sigma_{\mathrm{kl}}^{\mathrm{new}}(\mathrm{L})n_{\mathrm{l}} & \boldsymbol{n} \neq 0 \end{cases} \qquad (7)$$

where $\sigma_{\mathrm{ij}}^{\mathrm{new}}(\mathrm{K}) = C_{\mathrm{ijkl}}\varepsilon_{\mathrm{ij}}^{\mathrm{new}}(\mathrm{K})$, $\Omega_{\mathrm{ij}}^{-1}(\boldsymbol{n}) = C_{\mathrm{iklj}}n_{\mathrm{k}}n_{\mathrm{l}}$, and

$$\varepsilon_{\mathrm{kl}}^{\mathrm{new}}(\mathrm{K}) = \begin{cases} 1 & \text{if K is Voigt notation of kl} \\ 0 & \text{otherwise} \end{cases}$$

Kinetic equation

The following time-dependent Ginzburg-Landau equation[65] was used to describe the temporal and spatial evolution of the structural order parameters during the MT

$$\frac{d\eta_{\mathrm{p}}(\boldsymbol{r}, t)}{dt} = -M\frac{\delta F}{\delta\eta_{\mathrm{p}}(\boldsymbol{r}, t)} + \xi_{\mathrm{p}}(\boldsymbol{r}, t), \ \mathrm{p} = 1 \sim 12 \qquad (8)$$

where M is the kinetic coefficient and $\xi_p(\boldsymbol{r}, t)$ is the Langevin noise term for structural fluctuations, which meets the following fluctuation-dissipation theorem[66, 67]:

$$\langle \xi_{\mathrm{p}}(\boldsymbol{r}, t)\xi_{\mathrm{p}}(\boldsymbol{r}', t')\rangle = 2\frac{k_B T}{|\Delta f| l_0^3}\delta(\boldsymbol{r}-\boldsymbol{r}')\delta(t-t') \qquad (9)$$

where k_{B} is the Boltzmann constant, T is the absolute temperature, $|\Delta f|$=10^7 J/m^3 [68, 69] is the chemical driving force (free energy difference between the parent and martensitic phases calculated from the Landau free energy), $l_0 = 5$ nm is the length scale assigned to the computational grid increment, and δ is the Kronecker delta function.

Eq. (8) is solved numerically in the reciprocal space using a finite difference method for a compositionally modulated model system. The system size used in the simulations is $128l_0$×128 l_0×$128l_0$. Periodical boundary conditions were applied along all three dimensions.

Author Contributions

Z. P. L. and Y. W. initiated this project and design the experiments. F. Z, F. S. L, Y. Y, Y. Z. and Y. W. synthesized and characterized the samples. F. Z, F. S. L, Y. Y, Y. Z.and R. T. Q. performed the properties measurements. Z. H. N, Y. R. and Y. D. W. performed in-situ Synchrotron measurement. J. M. Z. and H. H. W. carried out the phase field simulations. Y. W. and Z. P. L. wrote and revised the paper. All the authors analyzed the data and contributed to the discussion and interpretation of the results.

CRediT authorship contribution statement

Yuan Wu: Conceptualization, Resources, Writing - review & editing, Methodology, Investigation, Visualization. **Fei Zhang, Fengshou Li,Yi Yang, Yao Zhang:** Investigation, Validation, Visualization. **Jiaming Zhu, Honghui Wu, Xiongjun Liu:** Software, Formal

analysis. **Ruitao Qu, Zhefeng Zhang**: Investigation. **Zhihua Nie, Yang Ren, Yandong Wang**: Resources, Investigation. **Hui Wang:** Project administration. **Zhaoping Lu:** Supervision, Conceptualization, Resources, Writing - review & editing, Funding acquisition.

Conflicts of interest

There are no conflicts to declare.

Supporting Information

Supporting Information is available.

Acknowledgements

This research was supported by National Natural Science Foundation of China (Nos. 11790293, 51871016, 52061135207, 51921001), 111 Project (B07003), the Program for Changjiang Scholars and Innovative Research Team in University of China (IRT_14R05) and the Fundamental Research Funds for the Central Universities. Use of the Advanced Photon Source is supported by the U.S. Department of Energy, USA, Office of Science, Office of Basic Energy Sciences, under Contract No. DE-AC02-06CH11357.

Notes and References

1 K. Otsuka and C. M. Wayman, *Shape memory materials*, Cambridge University Press, Cambridge 1999.

2 T. Duerig, A. Pelton and D. Stöckel, *Materials Science and Engineering A* 1999, **273-275**, 149-160.

3 K. Otsuka and X. Ren, *Prog. Mater Sci.*, 2005, **50**, 511-678.

4 S. Saadat, J. Salichs, M. Noori, Z. Hou, H. Davoodi, I. Bar-on, Y. Suzuki and A. Masuda, *Smart Mater. Struct.*, 2002, **11**, 218.

5 J. Lemaitre and J. L. Chaboche, *Mechanics of Solid Materials*, Cambridge University Press, 1994.

6 Y. Tanaka, Y. Himuro, R. Kainuma, Y. Sutou, T. Omori and K. Ishida, *Science*, 2010, **327**, 1488-1490.

7 T. Omori, K. Ando, M. Okano, X. Xu, Y. Tanaka, I. Ohnuma, R. Kainuma and K. Ishida, *Science*, 2011, **333**, 68-71.

8 J. Xia, Y. Noguchi, X. Xu, T. Odaira, Y. Kimura, M. Nagasako, T. Omori and R. Kainuma, *Science*, 2020, **369**, 855-858.

9 R. Dasgupta, *J. Mater. Res.*, 2014, **29**, 1681-1698.

10 J. Ma, I. Karaman and R. D. Noebe, *Int. Mater. Rev.*, 2010, **55**, 257-315.

11 V. Provenzano, A. J. Shapiro and R. D. Shull, *Nature*, 2004, **429**, 853-857.

12 Y. Song, X. Chen, V. Dabade, T. W. Shield and R. D. James, *Nature*, 2013, **502**, 85.

13 X. Ren and K. Otsuka, *Philos. Mag. A*, 2000, **80**, 467-491.

14 S. Sarkar, X. Ren and K. Otsuka, *Phys. Rev. Lett.*, 2005, **95**, 205702.

15 Y. Wang, X. Ren and K. Otsuka, *Phys. Rev. Lett.*, 2006, **97**, 225703.

16 Y. Wang, X. Ren, K. Otsuka and A. Saxena, *Acta Mater.*, 2008, **56**, 2885-2896.

17 Y. Wang, X. Ren, K. Otsuka and A. Saxena, *Phys. Rev. B*, 2007, **76**, 132201.

18 J. W. Yeh, S. K. Chen, S. J. Lin, J. Y. Gan, T. S. Chin, T. T. Shun, C. H. Tsau and S. Y. Chang, *Adv. Eng. Mater.*, 2004, **6**, 299-303.

19 Y. Zhang, T. T. Zuo, Z. Tang, M. C. Gao, K. A. Dahmen, P. K. Liaw and Z. P. Lu, *Prog. Mater. Sci.*, 2014, **61**, 1-93.

20 Q. Ding, Y. Zhang, X. Chen, X. Fu, D. Chen, S. Chen, L. Gu, F. Wei, H. Bei, Y. Gao, M. Wen, J. Li, Z. Zhang, T. Zhu, R. O. Ritchie and Q. Yu, *Nature*, 2019, **574**, 223-227.

21 Y. Bu, Y. Wu, Z. Lei, X. Yuan, H. Wu, X. Feng, J. Liu, J. Ding, Y. Lu, H. Wang, Z. Lu and W. Yang, *Mater. Today*, 2021, **46**, 28-34.

22 X. Chen, Q. Wang, Z. Cheng, M. Zhu, H. Zhou, P. Jiang, L. Zhou, Q. Xue, F. Yuan, J. Zhu, X. Wu and E. Ma, *Nature*, 2021, **592**, 712-716.

23 Z. Li, K. G. Pradeep, Y. Deng, D. Raabe and C. C. Tasan, *Nature*, 2016, **534**, 227-230.

24 F. X. Zhang, S. Zhao, K. Jin, H. Xue, G. Velisa, H. Bei, R. Huang, J. Y. P. Ko, D. C. Pagan, J. C. Neuefeind, W. J. Weber and Y. Zhang, *Phys. Rev. Lett.*, 2017, **118**, 205501.

25 J. Ding, Q. Yu, M. Asta and R. O. Ritchie, *Proc. Natl. Acad. Sci. U.S.A.*, 2018, **115**, 8919-8924.

26 N. Zhou, S. Jiang, T. Huang, M. Qin, T. Hu and J. Luo, *Sci. Bull.*, 2019, **64**, 856-864.

27 D. Canadinc, W. Trehern, J. Ma, I. Karaman, F. Sun and Z. Chaudhry, *Scripta Mater.*, 2019, **158**, 83-87.

28 G. S. Firstov, T. A. Kosorukova, Y. N. Koval and P. A. Verhovlyuk, *Shape Memory and Superelasticity*, 2015, **1**, 400-407.

29 C.-H. Chen and Y.-J. Chen, *Scripta Mater.*, 2019, **162**, 185-189.

30 Z. Xie, Y. Liu and J. Van Humbeeck, *Acta Mater.*, 1998, **46**, 1989-2000.

31 C. Biffi, M. Coduri and A. Tuissi, *Mater. Today Proceedinds*, 2015, **2**, S797-S800.

32 O. Levy, G. L. Hart and S. Curtarolo, *Acta Mater.*, 2010, **58**, 2887-2897.

33 Y. Ogawa, D. Ando, Y. Sutou and J. Koike, *Science*, 2016, **353**, 368-370.

34 Y. Hao, H. Wang, T. Li, J. Cairney, A. Ceguerra, Y. Wang, Y. Wang, D. Wang, E. Obbard and S. Li, *J. Mater. Sci. Technol.*, 2016, **32**, 705-709.

35 H. Kim, Y. Ikehara, J. Kim, H. Hosoda and S. Miyazaki, *Acta Mater.*, 2006, **54**, 2419-2429.

36 H. Pan, J. A. Ritter and P. B. Balbuena, *Langmuir*, 1998, **14**, 6323-6327.

37 R. Asaro and D. Barnett, *J. Mech. Phys. Solids*, 1975, **23**, 77-83.

38 T. Mori and K. Tanaka, *Acta Metall.*, 1973, **21**, 571-574.

39 Z. Zhang, Y. Wang, D. Wang, Y. Zhou, K. Otsuka and X. Ren, *Phys. Rev. B*, 2010, **81**, 224102.

40 N. Bordeaux, A. M. Montes-Arango, J. Liu, K. Barmak and L. H. Lewis, *Acta Mater.*, 2016, **103**, 608-615.

41 J. W. Seo and D. Schryvers, *Acta Mater.*, 1998, **46**, 1165-1175.

42 Y. Wu, D. Ma, Q. K. Li, A. D. Stoica, W. L. Song, H. Wang, X. J. Liu, G. M. Stoica, G. Y. Wang, K. An, X. L. Wang, M. Li and Z. P. Lu, *Acta Mater.*, 2017, **124**, 478-488.

43 T. Ungár, L. Balogh and G. Ribárik, *Metall. Mater. Trans. A*, 2010, **41**, 1202-1209.

44 Q. H. Zhang, Z. Zhai, Z. H. Nie, S. Harjo, D. Y. Cong, M. G. Wang, J. Li and Y. D. Wang, *J. Appl. Crystallogr.*, 2015, **48**, 1183-1191.

45 R. W. Cahn, P. Haasen, Physical Metallurgy. Fourth, revised and enhanced edition, North-Holland, 1996.

46 J. M. Zhu, H. H. Wu, X. S. Yang, H. Huang, T. Y. Zhang, Y. Z. Wang, S. Q. Shi, Dissecting the influence of nanoscale concentration modulation on martensitic transformation in multifunctional alloys. Acta Mater., 2019, **181**, 99-109.

47 M. Zarinejad, Y. Liu and T. J. White, *Intermetallics*, 2008, **16**, 876-883.

48 L. Rogal, P. Bobrowski, F. Körmann, S. Divinski, F. Stein and B. Grabowski, *Sci. Rep.*, 2017, **7**, 2209.

49 S. D. Wang, X. J. Liu, Z. F. Lei, D. Y. Lin, F. G. Bian, C. M. Yang, M. Y. Jiao, Q. Du, H. Wang, Y. Wu, S. H. Jiang, Z. P. Lu, Chemical short-range ordering and its strengthening effect in refractory high-entropy alloys. Phy. Rev. B 2021, **103**, 104107.

50 Y. Wu, F. Zhang, X. Y. Yuan, H. L. Huang, X. C. Wen, Y. H. Wang, M. Y. Zhang, H. H. Wu, X. J. Liu, Z. P. Lu. Short-range ordering and its effects on mechanical properties of high-entropy alloys. J. Mater. Sci. & Tech., 2021, **62**, 214-220.

51 L. Landau and E. Lifshitz, *Statistical Physics*, Pergamon Pres, Oxford, 1980.

52 J. W. Cahn and J. E. Hilliard, *J. Chem. Phys.*, 1958, **28**, 258-267.

53 J. W. Cahn and J. E. Hilliard, *J. Chem. Phys.*, 1959, **31**, 688-699.

54 A. Khachaturyan, *Theory of Structural Transformations in Solids*, John Wiley & Sons, New York, 1983.

55 J. Frenzel, A. Wieczorek, I. Opahle, B. Maaß, R. Drautz and G. Eggeler, *Acta Mater.*, 2015, **90**, 213-231.

56 J. Zhu, Y. Gao, D. Wang, T.-Y. Zhang and Y. Wang, *Acta Mater.*, 2017, **130**, 196-207.

57 R. J. Asaro and D. M. Barnett, *J. Mech. Phys. Solids*, 1975, **23**, 77-83.

58 H. E. Stanley, *Introduction to phase transitions and critical phenomena*, Oxford Unicersity Press, New York, 1971.

59 A. Hammersley, *J. Appl. Crystallogr.*, 2016, **49**, 646-652.

60 M. K. Miller, K. F. Russell, K. Thompson, R. Alvis and D. J. Larson, *Microsc. Microanal.*, 2007, **13**, 428-436.

61 K. Thompson, D. Lawrence, D. Larson, J. Olson, T. Kelly and B. Gorman, *Ultramicroscopy*, 2007, **107**, 131-139.

62 G. Firstov, A. Timoshevski, T. Kosorukova, Y. Koval, Y. Matviychuk and P. Verhovlyuk, *MATEC Web of Conferences*, 2015, **33**, 06006.

63 H. Y. Kim, Y. Ikehara, J. I. Kim, H. Hosoda and S. Miyazaki, *Acta Mater.*, 2006, **54**, 2419-2429.

64 T. Inamura, J. I. Kim, H. Y. Kim, H. Hosoda, K. Wakashima and S. Miyazaki, *Philos. Mag.*, 2007, **87**, 3325-3350.

65 J. D. Gunton, M. San Miguel and P. S. Sahni, in *Phase Transitiona and Critical Phemomena* ed. E. C. D. a. J. L. Lebowitz, Academic Press, London, 1983, vol. 8, pp. 269-466.

66 E. M. Lifshitz and L. P. Pitaevskii, in *Course Theor. Phys., 3rd ed.*, eds. L. Landau and E. Lifshitz, Pergamon Press, Oxford, 1980.

67 Y. Wang and A. G. Khachaturyan, *Acta Mater.*, 1997, **45**, 759-773.

68 J. Khalil-Allafi, W. W. Schmahl and T. Reinecke, *Smart Mater. Struct.*, 2005, **14**, S192-

S196.

69 G. B. Olson and M. Cohen, *Metall. Trans. A*, 1976, **7**, 1905-1914.